HHS Public Access

Author manuscript

J Magn Reson Imaging. Author manuscript; available in PMC 2016 November 01.

Published in final edited form as:

J Magn Reson Imaging. 2015 November ; 42(5): 1329–1338. doi:10.1002/jmri.24902.

Accuracy of 3D Dual Echo Steady State (DESS) MR Arthrography to Quantify Acetabular Cartilage Thickness

Christine L Abraham, PhD[1,2], **Neal K Bangerter, PhD**[3,4], **Lance S McGavin, BS**[2], **Christopher L Peters, MD**[2], **Alex J Drew, BS**[1,2], **Christopher J Hanrahan, MD, PhD**[3], and **Andrew E Anderson, PhD**[1,2]

[1]Department of Bioengineering, University of Utah, Salt Lake City, UT 84112

[2]Department of Orthopaedics, University of Utah, Salt Lake City, UT 84108

[3]Department of Radiology, University of Utah, Salt Lake City, UT 84108

[4]Department of Electrical and Computer Engineering, Brigham Young University, Provo, UT 84604

Abstract

Purpose—Clinical magnetic resonance imaging (MRI) sequences used to image hip cartilage often have reduced out-of-plane resolution and may lack adequate signal to noise to image cartilage. We deployed and quantified the accuracy of 3D dual echo steady state (DESS) MR arthrography with hip traction to image acetabular cartilage.

Methods—Saline was injected into four cadaver hips placed under traction. 3D DESS MRI scans were obtained before and after cores of cartilage were harvested from the acetabulum; the two MRIs were spatially aligned to reference core positions. The thickness of cartilage cores was measured under microscopy to serve as the reference standard. 3D reconstructions of cartilage and subchondral bone were generated using automatic and semi-automatic image segmentation. Cartilage thickness estimated from the 3D reconstructions was compared to physical measurements using Bland-Altman plots.

Results—As revealed by the automatic segmentation mask, saline imbibed the joint space throughout the articulating surface, with the exception of the posteroinferior region in two hips. Locations where air bubbles were introduced and regions of suspected low density bone disrupted an otherwise smooth automatic segmentation mask. Automatic and semi-automatic segmentation yielded a bias ± repeatability coefficient (95% limits of agreement) of 0.10 ± 0.51 mm (−0.41 to 0.61 mm) and 0.06 ± 0.43 mm (−0.37 to 0.49 mm), respectively.

Conclusions—Cartilage thickness can be estimated to within ~0.5 mm of the physical value with 95% confidence using 3D reconstructions of 3D DESS MR arthrography images. Manual correction of the automatic segmentation mask may improve reconstruction accuracy.

Corresponding Author: Andrew E Anderson, PhD, Department of Orthopaedics, University of Utah, 590 Wakara Way, Rm A100, Salt Lake City, UT 84108, Phone: 801-587-5208, aea4@utah.edu.

Keywords

hip; DESS MRI; cartilage thickness; cartilage imaging; osteoarthritis

INTRODUCTION

Hip osteoarthritis (OA) is a substantial economic and societal burden, affecting 9 million US citizens (1,2). Hip-preserving surgeries aim to prevent end-stage osteoarthritis and the need for hip arthroplasty in femoroacetabular impingement (FAI) and dysplasia patients by restoring normative bony coverage and contact mechanics (3–5). The success of surgery relies, in part, on an accurate pre-operative assessment of bone anatomy and cartilage thickness. The integrity and thickness of hyaline cartilage is particularly important as extensive damage or thinning to cartilage is a known contraindication for hip-preserving surgery (3,5). Radiographs are limited in their ability to discern subtle anatomical deformities, and do not provide detailed information of the hyaline cartilage thickness. With the addition of intra-articular contrast, CT arthrography provides images that have been shown to accurately visualize bone and cartilage (6,7). However, CT arthrography is limited primarily by the application of ionizing radiation, which is of concern with FAI and dysplasia patients as they typically present with symptoms in early adulthood and may require subsequent scans to evaluate possible progression of OA (4,8). Thus, MRI has become a widely used modality to assess cartilage thickness in patients with FAI and dysplasia.

Clinical MRI protocols of the hip typically acquire two-dimensional (2D) fast spin-echo (FSE) sequences (9,10). While 2D FSE sequences yield images with excellent tissue contrast and high in-plane spatial resolution, reduced out-of-plane resolution (i.e. thick image slices) may not visualize pathology due to partial volume averaging (11). Three-dimensional (3D) sequences minimize partial volume effects and through-plane distortion by acquiring thin, continuous image slices. With images acquired at nearly isotropic resolution, a 3D sequence can be post-processed to create any desired imaging plane. For example, radial MR slices, which are used to visualize anatomic deformities in the setting of FAI (12), can be reconstructed from a single 3D acquisition. Individual images can also be segmented and tessellated to display 3D osseous and cartilaginous surface anatomy for the purpose of planning surgery (13). Specifically, post-processing of these surfaces can yield maps of cartilage thickness that may isolate regions where cartilage is thin (6,13–15). Finally, 3D surfaces built from volumetric images provide the geometry for patient-specific computer models to estimate cartilage contact mechanics (e.g. finite element analyses) (16,17).

MRI of the hip is inherently challenging due to its deep location in the body and spherical geometry. Long scan times may be required to obtain images with sufficient resolution to minimize stair-case artifact and accurately visualize hip cartilage while still obtaining adequate signal to noise (SNR) in a joint surrounded by thick soft tissue (10,11). Additionally, the tight-fitting and congruent hip joint makes it difficult to distinguish opposing layers of cartilage. With improved technology and use of 3D gradient echo

imaging techniques that utilize small excitation pulses and short repetition times, 3D scans of the hip have been achieved in reasonable scan times (14,18–20). However, in these prior studies, resolution was limited or traction was not included, making it difficult to distinguish the boundary between acetabular and femoral cartilage (18–20).

Owed to its superior SNR and signal contrast previously demonstrated when imaging knee cartilage, 3D dual echo steady state (DESS) is a promising sequence to image the hip (18,21–26). 3D DESS can achieve nearly isotropic, high-resolution acquisitions in relatively short scan times. Also, using DESS, bone appears as negative signal, highlighting the potential of this protocol to image cartilage and bone in a single acquisition. With the addition of traction to separate acetabular and femoral cartilage, and intra-articular fluid to distinguish the joint space boundary, 3D DESS MRI could provide a feasible protocol to generate images of bone and cartilage in the hip. The objectives of this study were to: 1) deploy 3D DESS MR arthrography protocol with hip traction, and 2) using physical measurements of cartilage thickness as the reference standard, quantify the accuracy of acetabular cartilage thickness estimated from 3D surfaces segmented from the 3D DESS MR images.

METHODS

The general approach involved obtaining 3D DESS MRI scans of four intact cadaver hips before and after cores of cartilage were harvested from the acetabulum; the two MRIs were spatially aligned to reference positions of the cores. The thickness of each core was measured and compared to those obtained from the 3D reconstructions of the first MRI scan.

Injection, Traction, and Initial MRI Scan

In accordance with the University of Utah Institutional Review Board, two fresh-frozen pelvis to toe-tip cadavers (32 year female, 55 year male) were acquired (IRB#11755). Specimens were screened based on age less than 65 years, body mass index less than 25, no history of excessive smoking or drinking, absence of spinal and lower limb injury, and no history of hip osteoarthritis. To improve delineation between femoral and acetabular cartilage, a musculoskeletal radiologist (CJH) injected 25 ml sodium chloride 0.9% (saline) into each hip through a 22-gauge spinal needle using a lateral oblique approach. To allow saline to fill the joint space, bilateral traction was applied using a custom device made of polyvinylchloride tubing (Fig. 1). Traction was applied by first securing the pelvis to the proximal segment of the device using a wide strap. Next, a strap was attached to the ankle; an inferiorly directed force of approximately 5–10 kg was applied to the ankle by tightening a plastic cable tie that was fixed to the distal segment of the traction device (Fig. 1). The process of applying traction was repeated for the contralateral limb.

The pelvis and both hip joints were imaged using a 3.0-T magnet (Magnetom Trio; Siemens Medical Solutions, Erlangen, Germany) with a built in spine-matrix coil and body-matrix phased-array coil placed about the pelvic region. Three-dimensional MR images were acquired in the coronal plane using a water-excitation DESS sequence. The field-of-view of the scan encompassed the entire pelvis with an acquired voxel size of 0.5 × 0.5 × 0.7 mm. Imaging parameters included a repetition time of 16.3 ms, echo time of 4.7 ms, flip angle of

25°, and bandwidth of 186 Hz/pixel. Image acquisition time was 12 minutes using an acceleration factor of 2 with generalized autocalibrating partially parallel acquisition (GRAPPA).

Physical Measurements of Cored Cartilage Samples

After the first MRI, the acetabulum was accessed by incising the anterior and lateral hip/thigh soft tissue. The hip was dislocated by flexing and externally rotating the thigh with the ligamentum teres excised (27). Osteochondral cores were harvested from the acetabulum using a 5.3-mm trephine (Stryker Instruments, Kalamazoo, MI). The trephine was modified to include a center boring pin that facilitated removal of the plug (28). A total of 12 cores were acquired: 3 each from the anteroinferior, anterosuperior, posteroinferior, and posterosuperior regions (Fig. 2) (6,15,28).

Cores were bisected longitudinally using a custom miter-box to ensure equal division. Cores were positioned on a microscope stage (Nikon SMZ800, Nikon Instruments, NY) with the bisected side facing up and a stage micrometer in the field-of-view at the level of the bisected edge. Digital microscope images (Optronics Microscope Camera, Optronics, CA) were obtained of each bisected core at a magnification of 25× (Fig. 2). Each image was calibrated using the micrometer. Cartilage thickness was measured at the center of each core using ImageJ (29). Measurements of thickness for both halves of the core were averaged. Two observers (CLA and LSM, imaging scientists with 6 and 3 years' experience, respectively) measured cartilage thickness; nearly 2 weeks later, one observer (CLA) repeated the measurements.

Second MRI Scan

After harvesting cartilage cores from both hips, a second MRI was obtained to determine the position of the cores. Prior to this scan, saline-filled cylindrical tubes sized to match the core diameter were implanted in each cored hole to serve as fiducials. Extruded acrylic tubing with a quarter inch outer diameter was cut to 5 mm length segments. Circles templated to match the tubing diameter were laser cut from acrylic sheets to create the top and bottom components of the cylinder fiducials. An acrylic solvent bonded the cylinder bottoms, and a syringe filled the cylindrical cavity with saline before it was adhered to the top components.

After implanting fiducials, physiologic hip anatomy was restored by reducing the femoral head into the acetabulum and suturing the surrounding soft tissues. Traction was not necessary during the second scan as the joint capsule was not sealed and pressurized following dissection. The second MRI was acquired following the same imaging parameters as the first. Imaging was performed in the same orientation (Fig. 1). However, the traction frame and straps were not used.

MRI Post-Processing

Computational methods were used to quantify cartilage thickness from MR images (Fig. 3). Briefly, the acetabular cortex was segmented, reconstructed, and cropped equally in both MRIs. Next, the acetabular cortex from the first MRI was aligned to the acetabulum from the second scan. This transformation was applied to the acetabular cartilage, segmented

from the first MRI, to register the cartilage to the second MRI. With both acetabular cortex and cartilage surfaces transformed, the saline-filled fiducials defined the spatial location of each core. Cartilage thickness from the first scan was calculated at the appropriate locations, with details described below.

Segmentation and Three-dimensional Reconstruction—All segmentation and surface reconstructions were generated using Amira (5.4.5, Visage Imaging, San Diego, CA). First, image stacks were cropped to include those image slices that encompassed both hip joints and up-sampled using a Lanzcos filter kernel to improve the resolution of the segmentation mask (0.25 × 0.25 mm in-plane resolution, 0.23 mm thickness) (16). Pixels exclusively representing cortical bone, acetabular cartilage, and saline were selected in ImageJ (29) at a mid-joint axial image. These pixels defined intensity distributions to determine thresholds for segmentation. Thresholds were calculated as a weighted midpoint between maximum and minimum intensities. A weighted midpoint was chosen to account for pronounced differences between intensities that would otherwise overestimate brighter pixels, caused by volumetric averaging with adjacent pixels. Thresholds were determined for each hip and scan independently.

The ability of automatic and semi-automatic segmentation techniques to define cartilage anatomy was assessed separately. Specifically, the acetabular cartilage and the outer cortex of the acetabulum in the first MRI were segmented automatically by selecting the pixels within the predetermined thresholds as defined above. Next, a user manually edited the initial automatic mask for regions that did not, on qualitative inspection, appear to correctly define the cartilage-saline and/or cartilage-bone boundary. Two observers (CLA and LSM, imaging scientists with 6 and 3 years' experience, respectively) performed semi-automatic segmentation; observer CLA performed semi-automatic segmentation on two occasions, with a time lapse of two weeks. Inter- and intra-observer repeatability was assessed. The acetabular cortex and saline-filled fiducials were segmented and reconstructed from the second MRI scan in a similar manner. However, less soft tissue surrounded the hip joint in the second scan, which reduced SNR. Therefore, greater semi-automatic segmentation was required. All masks were reconstructed into 3D surfaces using built-in algorithms in Amira that applied controlled smoothing and decimation to reduce artifact.

Spherical Cropping—An objective approach was applied to align 3D surfaces from the first and second MRI. First, triangulated faces representing the articular region of the acetabular cortex were selected using first principal curvature as calculated in the FEBio software suite (30). From these selected faces, the radius and center of the best-fit sphere was calculated using a linear least-squares-optimization (30). This sphere was increased to a radius of 45 or 47 mm (smaller radius for female specimen) to define a boundary at which to crop the reconstructed cortex created from each MRI scan. With spherical cropping, the two triangulated reconstructions of the acetabular cortex could be aligned without bias introduced as a result of differences in the position of the hip in the MR scanner bed between successive scans.

Surface Alignment and Transformation—Once cropped, the two acetabular cortex surfaces were aligned using an iterative closest point algorithm built into Amira (Amira

MeshPack 5.4.5, Visage Imaging, San Diego, CA) that minimized the root mean square distance between surfaces. The transformation that aligned the first to second scan was applied to the acetabular cartilage reconstruction; the resulting surfaces of acetabular cartilage, acetabular cortex, and saline fiducials were then spatially positioned in the second MRI. The same transformation was used for each hip for both automatically and semi-automatically segmented reconstructions. By visualizing the surfaces together, regions where cartilage was cored (saline-filled fiducials) could be identified with respect to the reconstructions of the first scan.

Cartilage Thickness—The thickness of the reconstructed acetabular cartilage was determined using a validated algorithm (31). Briefly, the distance between cartilage and cortex surfaces was determined by projecting the surface normal vector of faces representing the subchondral bone boundary to the faces representing the outer surface of cartilage. Thickness was then mapped as a 3D color fringe plot, where each node that defined the surface of the reconstructed cartilage from the first MRI scan had a unique thickness value. Finally, cartilage thicknesses at nodes surrounding each saline-filled fiducial were averaged and compared to the thickness of the physically cored sample.

Qualitative Inspection, Data Analysis and Statistics

The initial mask provided by automatic segmentation was used to make qualitative assessments of the MR images acquired using the 3D DESS sequence. More specifically, using the automatic segmentation mask as a guide, regions where saline did not imbibe the joint space and locations where the mask did not follow what otherwise appeared to be boundaries for cartilage or subchondral bone were noted.

Inter- and intra-observer repeatability of physically measured cartilage and semi-automatic segmented MRI cartilage thickness were quantified using the intraclass correlation coefficient (ICC) (32). Inter-observer repeatability was assessed between the first set of measurements for both observers. Observer agreement was interpreted as: slight if the ICC < 0.20, fair if 0.21–0.40, moderate if 0.41–0.60, substantial if 0.61–0.80, and almost perfect if >0.80 (33). For subsequent analysis, the physical and semi-automatic segmented MRI thickness measurements from both observers (CLA measures 1 and 2, LSM measure 1) were averaged.

Bland-Altman plots assessed agreement between MRI-based estimates of cartilage thickness and physical measurements (34). Bias, defined as the average difference between measurement techniques, was calculated to define accuracy. The repeatability coefficient, determined by multiplying the standard deviation of the differences by 1.96, provided a measurement of precision. Finally, 95% limits of agreement (bias ± repeatability coefficient) were quantified as an additional measure of precision (35). Results for MRI cartilage thickness determined with automatic and semi-automatic segmentation were presented separately. Bland-Altman plots were generated using SigmaPlot (v 11.0; Systat Software, San Jose, CA).

To account for clustered data at the level of each hip (n = 4) and cadaver (n = 2), the variance was adjusted using the design effect. The corrected variance was multiplied by the

design effect, DE: DE = 1+ (n−1)(ICC), where n was the average cluster size and the ICC was computed at the hip level and cadaver level of clustering (6,36). Both ICCs were zero when truncated to six decimal places. Therefore, the variance was not increased and conventional statistical methods that assume independence of observations were applied.

RESULTS

Upon inspection of the automatic segmentation mask, saline was found to imbibe the joint space throughout most of the articulating surface of all hips (Fig. 4), with the exception of the posteroinferior region in two hips (Fig. 5). Both the cartilaginous and osseous boundaries of all hips appeared to be a smooth curve as evident by the automatic mask (Fig. 4), but exceptions were noted. Specifically, the automatic mask transitioned abruptly and was unable to follow what appeared to be the boundary of subchondral bone and cartilage in the posteroinferior region of one hip (Fig. 5). Also, air bubbles were introduced in two hips at the anterior injection site, again causing an abrupt transition in the automatic mask (Fig. 5). Finally, areas of suspected low bone density appeared as a broken segmentation mask in two hips (Fig. 5). Manual correction was applied in these regions (Fig. 5), but was not required elsewhere.

As measured experimentally, cored cartilage thickness ranged from 0.80 to 2.95 mm (mean, 1.51 ± 0.49), compared to 0.76 to 3.21 mm (mean, 1.60 ± 0.50) and 0.77 to 3.20 mm (mean, 1.56 ± 0.50) as estimated from MRI reconstructions with automatic and semi-automatic segmentation, respectively. Acetabular reconstructions with cartilage thickness plotted demonstrated that cartilage at the superolateral acetabulum was approximately 1.5 mm thicker than cartilage at the medial aspect of the posterior region for all four hips analyzed (Fig. 6). Also, cartilage along the lateral rim was approximately 2.5 mm thicker than the cartilage found in the most medial aspect of the acetabulum.

Cartilage was reconstructed with automatic segmentation to a bias of 0.10 mm and repeatability coefficient of ± 0.51 mm. Using semi-automatic segmentation, the bias improved to 0.06 mm, as did the repeatability coefficient at ± 0.43 mm. Bland-Altman plots demonstrated uniform scatter. With no proportional bias, 95% limits of agreement were −0.41 to 0.61 mm for automatic and −0.37 to 0.49 mm for semi-automatic segmentation (Fig. 7).

Inter- and intra-observer repeatability of cartilage thickness as measured from microscope images and estimated from reconstructions generated from semi-automatically segmented MRI images were almost perfect. For microscope measurements, inter- and intra-observer ICC values were 0.948 and 0.950, respectively, and for semi-automatically segmented MRI thicknesses, 0.968 and 0.940, respectively.

DISCUSSION

This study demonstrated that the chosen 3D DESS MRI protocol for the hip that included traction and intra-articular saline yielded images that could be defined with an automatic segmentation mask throughout most of the articulating surface of the acetabulum. Using both automatic and semi-automatic segmentation techniques, acetabular cartilage thickness

from the 3D reconstructions could be estimated within ~0.5 mm of the physical measurements with 95% confidence. Areas where the automatic segmentation mask transitioned abruptly were confined to the posteroinferior region where bone was suspected to be of low density and the anterior compartment of the hip when air bubbles were present. Outside these regions, manual correction of the automatic mask was not necessary to create 3D surfaces of bone and cartilage. If successfully applied to living subjects, the described 3D DESS MRI protocol may help to plan treatment strategies for patients who are candidates for hip preservation surgery.

The acetabular cartilage thickness profiles and average thickness of 1.51 ± 0.49 mm found in our study are consistent with previous findings (6,7,14,15,37–39). Using MRA, Nishii et al. reported an average acetabular cartilage thickness of 1.91 mm, ranging from 1.1 to 4.0 mm, as measured from digitized anatomic slices in 4 cadaveric hips (14). Also, a study of 10 cadaveric hips measured average acetabular cartilage thicknesses ranging from 1.06 ± 0.24 mm in the posteromedial acetabulum to 1.83 ± 0.45 mm in the superolateral acetabulum (37). From cartilage thickness plots, our findings concur with Shepherd and Seedhom that thinner cartilage is located medially, and the thickest cartilage is located in the superolateral acetabulum (6,14,37,38).

As reported to date, the most accurate methods described for imaging acetabular cartilage thickness have used surface reconstructions to calculate thickness rather than pixel-based measurement of thickness on image slices (6,7,14,15,40). Studies by Wyler et al. and Hodler et al. measured thickness on 2D images and concluded that hip cartilage thickness could not be accurately determined in at least half of MR images (7,14,40). Errors in referencing anatomic slice measurements to their respective image-based locations as well as the limitation of measurement accuracy from in-plane scan resolution likely explain the reduced accuracy with measurements made on image slices. Also, smoothing and decimation of a surface generated from voxel-based images inherently removes noise. This may explain why our accuracy measurements represent an improvement to prior studies that utilized single images to quantify cartilage thickness (7,14,40).

Allen et al. and Tamura et al. utilized 3D reconstructions of CT arthrographic images to estimate acetabular cartilage thickness; their results are the most accurate to date (6,15). The bias and 95% limits of agreement for semi-automatic segmentation using DESS MRI in our study (0.06 ± 0.43 mm) represents a slight improvement compared to Allen et al. (0.13 ± 0.46 mm) and Tamura et al. (0.18 ± 0.75 mm). A validation study by Nishii et al. determined the mean error of measurements from surface reconstructions generated from MRI as 0.28 ± 0.23 mm (14). Though each of these studies utilized 3D models, we believe our results demonstrate superior accuracy because we acquired higher resolution scans and up-sampled images for segmentation. For example, Nishii et al. utilized a 0.625 mm in-plane and 1.5 mm out-of-plane resolution compared to the 0.5 mm in-plane and 0.7 mm out-of-plane resolution utilized herein.

In our study, MRI measurements based on automatic and semi-automatic segmentation had similar accuracy when compared to physical thickness of cored specimens. Nevertheless, semi-automatic segmentation was associated with improved accuracy, evidenced by tighter

95% limits of agreement. The fact that automatic segmentation did not identify the correct boundaries in all locations where cartilage was cored explains why semi-automatic segmentation improved the accuracy. Our study highlights the importance of eliminating air bubbles and use of traction to enable saline to imbibe the entire joint space. The area suspected to have low subchondral bone density as the cause for segmentation error also suggests that subchondral bone should be sufficiently intact to obtain accurate measurements of cartilage thickness using 3D DESS.

There are several potential benefits to the described 3D DESS MR imaging protocol. First, as with any MR sequence, there is no exposure to ionizing radiation. Second, the accuracy of cartilage thickness measurements reported from this sequence is highest for MRI reported to date and is as good or better than CT arthrography (6,15). Third, inclusion of traction enabled separation of acetabular from femoral cartilage. Clinically, it is important to assess femoral and acetabular cartilage independently. For example, femoral cartilage thinning is typically indicative of advanced damage as deterioration of the acetabular cartilage usually precedes femoral cartilage deterioration (4,41). Therefore, consistent with the literature, we believe traction is a necessary component for imaging studies of the hip (17).

Acetabular cartilage thickness could be measured at discrete locations on a single image slice from the 3D DESS MR sequence. However, for diagnostic information and surgical planning, we believe 3D reconstructions of the bone cortex and cartilage provide more descriptive data to guide treatment planning. Fringe plots of cartilage thickness, visualized relative to the bony anatomy in 3D, could elucidate regions of thin cartilage that would help surgeons to choose between hip arthroplasty and hip-preserving surgery. It has been shown that predictions of cartilage contact stress by patient-specific finite element models are sensitive to changes in the thickness of cartilage as portrayed in the model (42). Therefore, beyond clinical assessments, having the ability to create 3D reconstructions of cartilage from MRI could increase the accuracy of computer models.

Using CT arthrography, the attenuation of cortical bone closely represents that of the intra-articular radio-opaque contrast injected into the joint capsule. As a result, CT arthrographic images of the hip require substantial manual correction of segmentation to distinguish the bone-contrast boundary to create 3D models (16). In contrast, DESS MR images delineate bone cartilage, and injected saline at varying gray-levels as highlighted by automatic segmentation. Thus, use of DESS MRI may automate the process to generate 3D surface models for important structures of the hip.

There are some limitations with this study. First, the sample size was small, with a total 4 hips. Also, post-processing of the MR images may have introduced error with the alignment procedure used to relate the first and second scans. Because bone and cartilage surfaces are generally smooth in the articulating region, we would not expect pronounced changes in thickness at the immediate regions identified by saline fiducials. Therefore, small errors in locating the spatial position of the cartilage cores would conceivably have minimal effect on the accuracy of measurements. Our approach to measure acetabular thickness relied on segmentation of the cartilage-subchondral bone boundary, but we did not explicitly quantify the accuracy of DESS MRI to measure bone anatomy. However, given the favorable results

herein, we believe DESS MRI can delineate the cartilage-subchondral bone boundary. Future studies will need to assess the accuracy of DESS MRI for measuring the thickness of subchondral and cortical bone. Finally, this study measured cartilage thickness in cadaver hip joints that did not show evidence of cartilage damage or thinning. Therefore, the results may not be relevant to those hips with severe cartilage thinning. However, the protocol may be appropriate for evaluating candidates for hip-preserving surgery.

Our study simulated patient imaging as closely as possible by scanning intact pelvis to toe-tip specimens to obtain cartilage thickness maps. Translating this protocol into live subjects may be a challenge due to motion artifact and need for extended hip traction. However, a recent study that employed traction with a 2D MRI scan demonstrates the feasibility of using traction during an MR scan to visualize both layers of articular cartilage (43). In the future, we will incorporate methods to minimize motion artifact by scanning each hip separately and will also adopt techniques to stabilize the hip during traction despite possible muscular co-contraction.

In summary, using both automatic and semi-automatic segmentation, acetabular cartilage thickness from 3D reconstructions of DESS MR images could be estimated within ~0.5 mm of the physical measurements with 95% confidence. Historically, use of cumbersome methods and/or custom software to segment MRI images, such as cubic or quadratic splines (44), has likely been a factor that has hindered the widespread deployment of pre-operative models to facilitate operative decision making for patients with hip abnormalities. As we demonstrated here, use of automatic segmentation of cartilage and subchondral bone with commercially available software provides a level of accuracy that is very similar to semi-automatic segmentation. By using basic, threshold-based automatic segmentation of 3D DESS MR images, it may be possible to generate pre-operative models that visualize 3D cartilage and bone anatomy within a reasonable time frame. The extent to which such an analysis would benefit the clinician is not yet known, but the results of our study provide a protocol to be extended to living subjects. Though there will be additional challenges to overcome when deploying 3D DESS for live patients, the accuracy results reported in the in vitro setting herein are promising as they represent the highest reported accuracy of cartilage thickness measurements from the available volumetric imaging modalities, including CT arthrography.

Acknowledgments

Financial support from NIH #R01AR053344 and the University of Utah Funding Incentive Seed Grant Program is gratefully acknowledged. These funding agencies had no role in study design; data collection, analysis or interpretation; manuscript writing; or the decision to submit the manuscript.

References

1. Felson DT. Do occupation-related physical factors contribute to arthritis? Baillieres Clin Rheumatol. 1994; 8:63–77. [PubMed: 8149450]
2. Murphy LB, Helmick CG, Schwartz TA, et al. One in four people may develop symptomatic hip osteoarthritis in his or her lifetime. Osteoarthritis Cartilage. 2010; 18:1372–1379. [PubMed: 20713163]

3. Clohisy JC, Knaus ER, Hunt DM, Lesher JM, Harris-Hayes M, Prather H. Clinical presentation of patients with symptomatic anterior hip impingement. Clin Orthop Relat Res. 2009; 467:638–644. [PubMed: 19130160]
4. Ganz R, Leunig M, Leunig-Ganz K, Harris WH. The etiology of osteoarthritis of the hip: an integrated mechanical concept. Clin Orthop Relat Res. 2008; 466:264–272. [PubMed: 18196405]
5. Cunningham T, Jessel R, Zurakowski D, Millis MB, Kim YJ. Delayed gadolinium-enhanced magnetic resonance imaging of cartilage to predict early failure of Bernese periacetabular osteotomy for hip dysplasia. J Bone Joint Surg Am. 2006; 88:1540–1548. [PubMed: 16818980]
6. Allen BC, Peters CL, Brown NA, Anderson AE. Acetabular cartilage thickness: accuracy of three-dimensional reconstructions from multidetector CT arthrograms in a cadaver study. Radiology. 2010; 255:544–552. [PubMed: 20413764]
7. Wyler A, Bousson V, Bergot C, et al. Comparison of MR-arthrography and CT-arthrography in hyaline cartilage-thickness measurement in radiographically normal cadaver hips with anatomy as gold standard. Osteoarthritis Cartilage. 2009; 17:19–25. [PubMed: 18614381]
8. Clohisy JC, Dobson MA, Robison JF, et al. Radiographic structural abnormalities associated with premature, natural hip-joint failure. J Bone Joint Surg Am. 2011; 93 (Suppl 2):3–9. [PubMed: 21543681]
9. Gold SL, Burge AJ, Potter HG. MRI of hip cartilage: joint morphology, structure, and composition. Clin Orthop Relat Res. 2012; 470:3321–3331. [PubMed: 22723242]
10. Mamisch TC, Bittersohl B, Hughes T, et al. Magnetic resonance imaging of the hip at 3 Tesla: clinical value in femoroacetabular impingement of the hip and current concepts. Semin Musculoskelet Radiol. 2008; 12:212–222. [PubMed: 18850503]
11. Kijowski R, Gold GE. Routine 3D magnetic resonance imaging of joints. J Magn Reson Imaging. 2011; 33:758–771. [PubMed: 21448939]
12. Rakhra KS, Sheikh AM, Allen D, Beaule PE. Comparison of MRI alpha angle measurement planes in femoroacetabular impingement. Clinical orthopaedics and related research. 2009; 467:660–665. [PubMed: 19037709]
13. Peters CL, Erickson JA, Anderson L, Anderson AA, Weiss J. Hip-preserving surgery: understanding complex pathomorphology. J Bone Joint Surg Am. 2009; 91 (Suppl 6):42–58. [PubMed: 19884411]
14. Nishii T, Sugano N, Sato Y, Tanaka H, Miki H, Yoshikawa H. Three-dimensional distribution of acetabular cartilage thickness in patients with hip dysplasia: a fully automated computational analysis of MR imaging. Osteoarthritis Cartilage. 2004; 12:650–657. [PubMed: 15262245]
15. Tamura S, Nishii T, Shiomi T, et al. Three-dimensional patterns of early acetabular cartilage damage in hip dysplasia; a high-resolutional CT arthrography study. Osteoarthritis Cartilage. 2012; 20:646–652. [PubMed: 22469852]
16. Harris MD, Anderson AE, Henak CR, Ellis BJ, Peters CL, Weiss JA. Finite element prediction of cartilage contact stresses in normal human hips. J Orthop Res. 2012; 30:1133–1139. [PubMed: 22213112]
17. Henak CR, Abraham CL, Peters CL, Sanders RK, Weiss JA, Anderson AE. Computed tomography arthrography with traction in the human hip for three-dimensional reconstruction of cartilage and the acetabular labrum. Clinical radiology. 2014; 69:e381–391. [PubMed: 25070373]
18. Ellermann J, Ziegler C, Nissi MJ, et al. Acetabular cartilage assessment in patients with femoroacetabular impingement by using T2* mapping with arthroscopic verification. Radiology. 2014; 271:512–523. [PubMed: 24520945]
19. Stelzeneder D, Mamisch TC, Kress I, et al. Patterns of joint damage seen on MRI in early hip osteoarthritis due to structural hip deformities. Osteoarthritis Cartilage. 2012; 20:661–669. [PubMed: 22469848]
20. Apprich S, Mamisch TC, Welsch GH, et al. Evaluation of articular cartilage in patients with femoroacetabular impingement (FAI) using T2* mapping at different time points at 3. 0 Tesla MRI: a feasibility study. Skeletal Radiol. 2012; 41:987–995. [PubMed: 22057581]
21. Duc SR, Pfirrmann CW, Schmid MR, et al. Articular cartilage defects detected with 3D water-excitation true FISP: prospective comparison with sequences commonly used for knee imaging. Radiology. 2007; 245:216–223. [PubMed: 17717327]

22. Eckstein F, Cicuttini F, Raynauld JP, Waterton JC, Peterfy C. Magnetic resonance imaging (MRI) of articular cartilage in knee osteoarthritis (OA): morphological assessment. Osteoarthritis Cartilage. 2006; 14 (Suppl A):A46–75. [PubMed: 16713720]
23. Friedrich KM, Reiter G, Kaiser B, et al. High-resolution cartilage imaging of the knee at 3T: basic evaluation of modern isotropic 3D MR-sequences. Eur J Radiol. 2011; 78:398–405. [PubMed: 20138723]
24. Knuesel PR, Pfirrmann CW, Noetzli HP, et al. MR arthrography of the hip: diagnostic performance of a dedicated water-excitation 3D double-echo steady-state sequence to detect cartilage lesions. AJR Am J Roentgenol. 2004; 183:1729–1735. [PubMed: 15547220]
25. Sutter R, Zubler V, Hoffmann A, et al. Hip MRI: how useful is intraarticular contrast material for evaluating surgically proven lesions of the labrum and articular cartilage? AJR Am J Roentgenol. 2014; 202:160–169. [PubMed: 24370140]
26. Wirth W, Nevitt M, Hellio Le Graverand MP, et al. Sensitivity to change of cartilage morphometry using coronal FLASH, sagittal DESS, and coronal MPR DESS protocols--comparative data from the Osteoarthritis Initiative (OAI). Osteoarthritis Cartilage. 2010; 18:547–554. [PubMed: 20060948]
27. Ganz R, Gill TJ, Gautier E, Ganz K, Krugel N, Berlemann U. Surgical dislocation of the adult hip a technique with full access to the femoral head and acetabulum without the risk of avascular necrosis. J Bone Joint Surg Br. 2001; 83:1119–1124. [PubMed: 11764423]
28. El-Khoury GY, Alliman KJ, Lundberg HJ, Rudert MJ, Brown TD, Saltzman CL. Cartilage thickness in cadaveric ankles: measurement with double-contrast multi-detector row CT arthrography versus MR imaging. Radiology. 2004; 233:768–773. [PubMed: 15516604]
29. Schneider CA, Rasband WS, Eliceiri KW. NIH Image to ImageJ: 25 years of image analysis. Nat Methods. 2012; 9:671–675. [PubMed: 22930834]
30. Maas SA, Ellis BJ, Ateshian GA, Weiss JA. FEBio: finite elements for biomechanics. J Biomech Eng. 2012; 134:011005. [PubMed: 22482660]
31. Anderson AE, Peters CL, Tuttle BD, Weiss JA. Subject-specific finite element model of the pelvis: development, validation and sensitivity studies. J Biomech Eng. 2005; 127:364–373. [PubMed: 16060343]
32. Streiner, D.; Norman, G. Health Measurement scales: A practical guide to their development and use. Oxford, England: Oxford University Press; 1995.
33. Landis JR, Koch GG. The measurement of observer agreement for categorical data. Biometrics. 1977; 33:159–174. [PubMed: 843571]
34. Bland JM, Altman DG. Statistical methods for assessing agreement between two methods of clinical measurement. Lancet. 1986; 1:307–310. [PubMed: 2868172]
35. Mantha S, Roizen MF, Fleisher LA, Thisted R, Foss J. Comparing methods of clinical measurement: reporting standards for bland and altman analysis. Anesth Analg. 2000; 90:593–602. [PubMed: 10702443]
36. McCarthy W, Thompson DR. The Analysis of Pixel Intensity (Myocardial Signal Density) Data: The Quantification of Myocardial Perfusion by Imaging Methods. COBRA Preprint Series. 2007 Working Paper 23.
37. Athanasiou KA, Agarwal A, Dzida FJ. Comparative study of the intrinsic mechanical properties of the human acetabular and femoral head cartilage. J Orthop Res. 1994; 12:340–349. [PubMed: 8207587]
38. Shepherd DE, Seedhom BB. Thickness of human articular cartilage in joints of the lower limb. Ann Rheum Dis. 1999; 58:27–34. [PubMed: 10343537]
39. von Eisenhart R, Adam C, Steinlechner M, Muller-Gerbl M, Eckstein F. Quantitative determination of joint incongruity and pressure distribution during simulated gait and cartilage thickness in the human hip joint. J Orthop Res. 1999; 17:532–539. [PubMed: 10459759]
40. Hodler J, Trudell D, Pathria MN, Resnick D. Width of the articular cartilage of the hip: quantification by using fat-suppression spin-echo MR imaging in cadavers. AJR Am J Roentgenol. 1992; 159:351–355. [PubMed: 1632354]

41. Redmond JM, Gupta A, Stake CE, Domb BG. The prevalence of hip labral and chondral lesions identified by method of detection during periacetabular osteotomy: arthroscopy versus arthrotomy. Arthroscopy. 2014; 30:382–388. [PubMed: 24461141]

42. Anderson AE, Ellis BJ, Maas SA, Weiss JA. Effects of idealized joint geometry on finite element predictions of cartilage contact stresses in the hip. J Biomech. 2010; 43:1351–1357. [PubMed: 20176359]

43. Schmaranzer F, Klauser A, Kogler M, et al. Improving visualization of the central compartment of the hip with direct MR arthrography under axial leg traction: a feasibility study. Academic radiology. 2014; 21:1240–1247. [PubMed: 24981959]

44. Stammberger T, Eckstein F, Michaelis M, Englmeier KH, Reiser M. Interobserver reproducibility of quantitative cartilage measurements: comparison of B-spline snakes and manual segmentation. Magnetic resonance imaging. 1999; 17:1033–1042. [PubMed: 10463654]

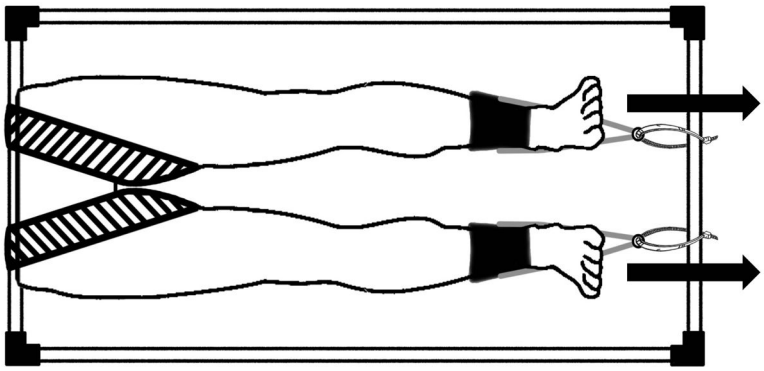

Figure 1.

Schematic of custom traction frame made of polyvinylchloride. The proximal segment of the pelvis was secured to the traction device using wide Velcro™ belts. Bilateral traction was applied through straps attached to the ankles. An inferiorly directed force (indicated by arrows) was applied to each ankle strap with a plastic cable tie that was then fixed to the distal segment of the traction device. *Column Width, Grayscale.*

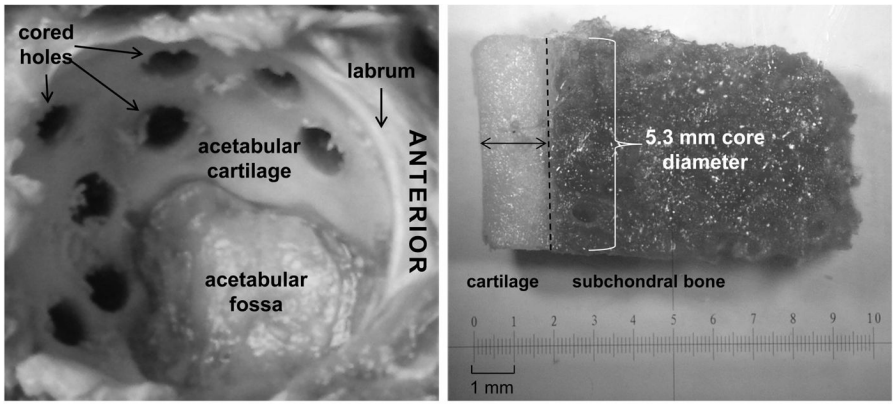

Figure 2.

Photographs of acetabulum and core of cartilage. Left panel-exposed acetabulum after 5.3 mm cartilage cores were harvested. Right panel-digital microscope image of bisected core with micrometer at 25× magnification. The dashed line labels the bone-cartilage interface and the arrows indicate cartilage thickness measurement. *Page Width, Grayscale.*

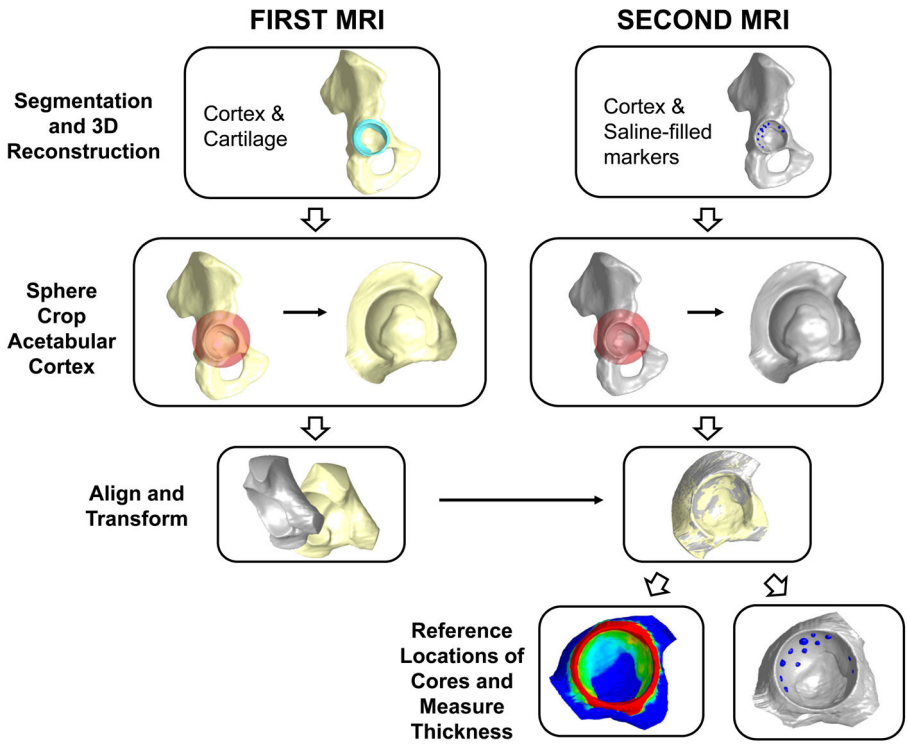

Figure 3.

MRI post-processing workflow. Analysis for the first and second MRI (separated by columns) occurred at distinct stages (separated by rows), including segmentation and generation of surfaces and ending with the determination of cartilage thickness at marker locations. *Page Width, Color*.

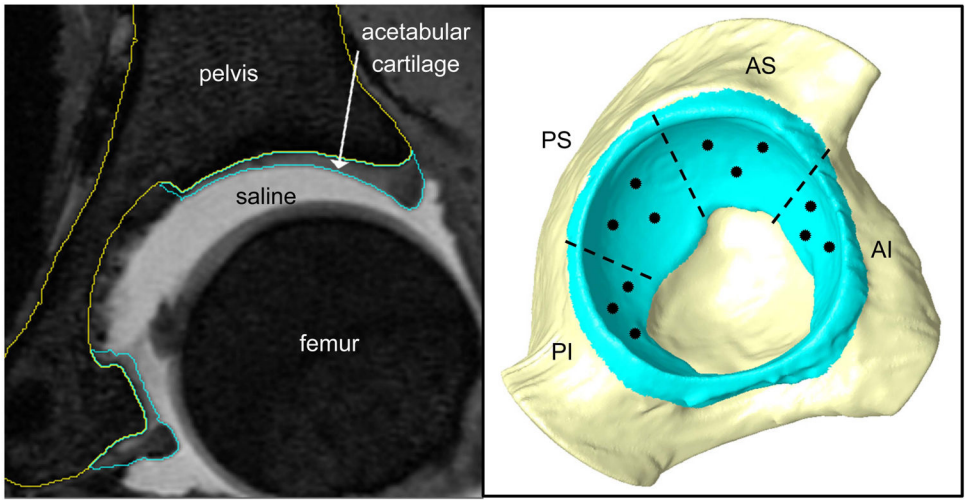

Figure 4.

Sample DESS image with three-dimensional reconstruction. Left panel-mid-joint coronal slice of DESS MRI with bone, cartilage, and saline clearly visualized. The acetabular cortex and cartilage automatically defined segmentation masks are outlined in yellow and blue, respectively. Right panel-lateral view of surface reconstruction of acetabular cortex and cartilage with posteroinferior (PI), posterosuperior (PS), anterosuperior (AS), anteroinferior (AI) regions identified and approximate locations of cartilage cores shown. *Page Width, Color.*

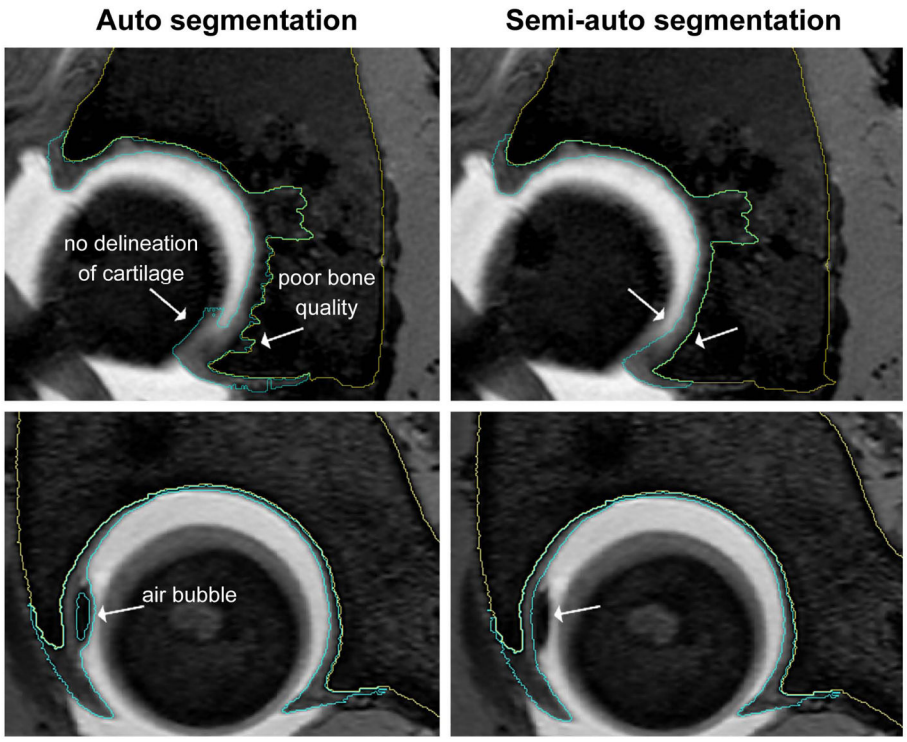

Figure 5.

Regions where automatic segmentation failed to delineate bone-cartilage and cartilage-saline boundaries. Upper left-shown at a posterior coronal slice, automatic segmentation did not properly identify the bone-cartilage boundary in regions of suspected low bone density and cartilage-saline boundary where saline failed to imbibe the joint space. Upper right-manual correction of the same coronal image in the upper left was used to better-define the bone and cartilage boundary. Lower left-shown at a sagittal image near the medial wall of the femur, an air bubble introduced into the anterior joint space prevented automatic segmentation of cartilage. Lower right-semi-automatic segmentation of the same sagittal image in the lower left panel corrected the site of the air bubble as indicated by the arrow. *Page Width, Color*.

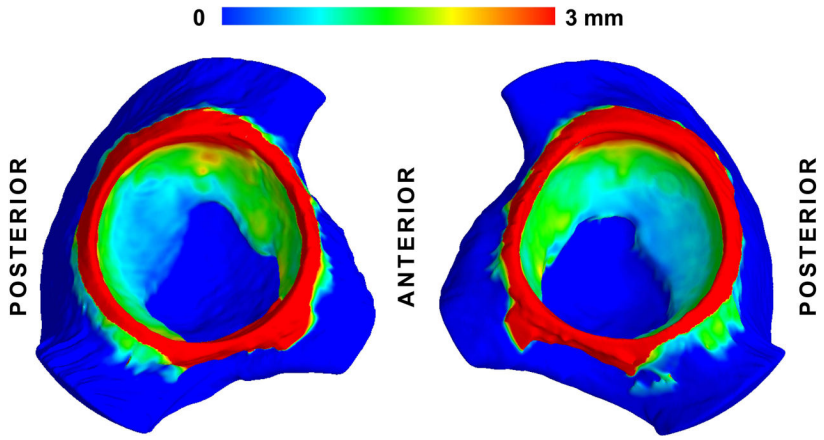

Figure 6.

Cartilage thickness plots of both hips from one cadaver. The labrum was included in the cartilage surface reconstructions, and is much thicker than articular cartilage (indicated by the red color on the thickness plot); analysis of the thickness of the labrum was not performed. The thickest and thinnest cartilage was observed in the superolateral and posteromedial acetabulum, respectively. *Page Width, Color.*

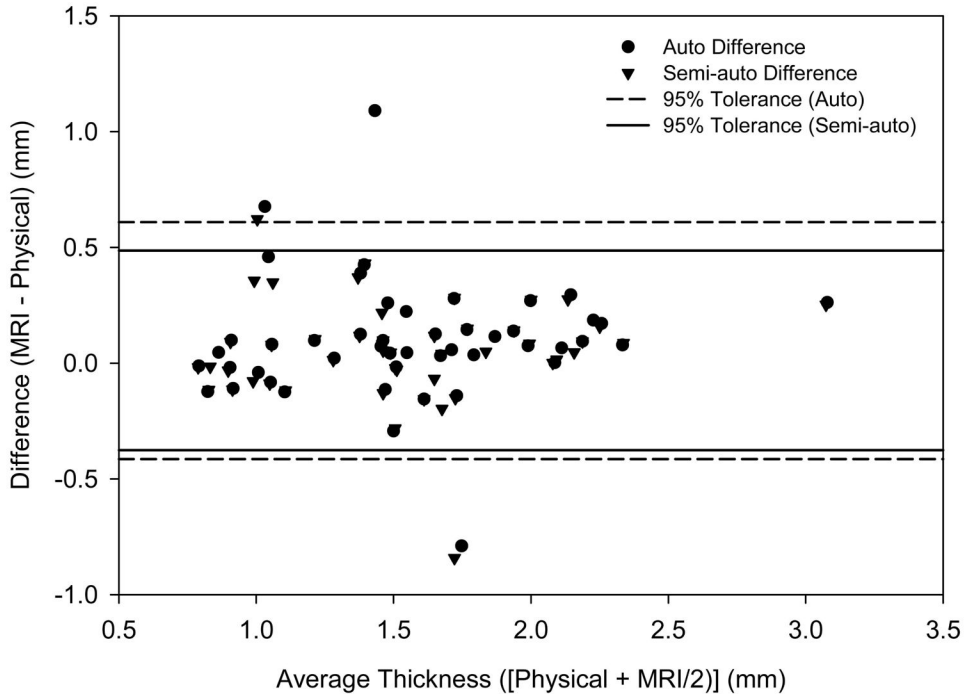

Figure 7.

Bland Altman plots to assess the accuracy of automatic and semi-automatic segmentation. The average thickness of physical and MRI measurement are plotted against the difference between physical and MRI measurements. Automatic and semi-automatic points are indicated by circles and triangles, respectively. Improved accuracy of semi-automatic segmentation is evidenced by tighter 95% tolerance limits for semi-automatic segmentation (solid lines) compared to those of automatic segmentation (dashed lines). *Column Width, Grayscale.*